

AD \_\_\_\_\_

Award Number: W81XWH-10-1-0713

TITLE: Magnetic Resonance Characterization of Axonal Response to Spinal Cord Injury

PRINCIPAL INVESTIGATOR: David B Hackney

CONTRACTING ORGANIZATION: Beth Israel Deaconess Medical Center  
Boston, MA 02215

REPORT DATE: October 2012

TYPE OF REPORT: Annual

PREPARED FOR: U.S. Army Medical Research and Materiel Command  
Fort Detrick, Maryland 21702-5012

DISTRIBUTION STATEMENT: Approved for Public Release;  
Distribution Unlimited

The views, opinions and/or findings contained in this report are those of the author(s) and should not be construed as an official Department of the Army position, policy or decision unless so designated by other documentation.

REPORT DOCUMENTATION PAGE				Form Approved OMB No. 0704-0188	
Public reporting burden for this collection of information is estimated to average 1 hour per response, including the time for reviewing instructions, searching existing data sources, gathering and maintaining the data needed, and completing and reviewing this collection of information. Send comments regarding this burden estimate or any other aspect of this collection of information, including suggestions for reducing this burden to Department of Defense, Washington Headquarters Services, Directorate for Information Operations and Reports (0704-0188), 1215 Jefferson Davis Highway, Suite 1204, Arlington, VA 22202-4302. Respondents should be aware that notwithstanding any other provision of law, no person shall be subject to any penalty for failing to comply with a collection of information if it does not display a currently valid OMB control number. <b>PLEASE DO NOT RETURN YOUR FORM TO THE ABOVE ADDRESS.</b>					
1. REPORT DATE October 2012		2. REPORT TYPE Annual		3. DATES COVERED 27 Sept 2011- 26 Sept 2012	
4. TITLE AND SUBTITLE Magnetic Resonance Characterization of Axonal Response to Spinal Cord Injury				5a. CONTRACT NUMBER	
				5b. GRANT NUMBER W81XWH-10-1-0713	
				5c. PROGRAM ELEMENT NUMBER	
6. AUTHOR(S) David B Hackney				5d. PROJECT NUMBER	
				5e. TASK NUMBER	
				5f. WORK UNIT NUMBER	
7. PERFORMING ORGANIZATION NAME(S) AND ADDRESS(ES) Beth Israel Deaconess Medical Center, Boston, MA 02215				8. PERFORMING ORGANIZATION REPORT NUMBER	
9. SPONSORING / MONITORING AGENCY NAME(S) AND ADDRESS(ES) U.S. Army Medical Research and Materiel Command Fort Detrick, Maryland 21702-5012				10. SPONSOR/MONITOR'S ACRONYM(S)	
				11. SPONSOR/MONITOR'S REPORT NUMBER(S)	
12. DISTRIBUTION / AVAILABILITY STATEMENT Approved for Public Release; Distribution Unlimited					
13. SUPPLEMENTARY NOTES					
14. ABSTRACT Our overall goal is to <b>characterize axonal and myelin damage in human spinal cord injury</b> , its evolution over time, and response to therapy. Towards this end, we have developed a set of <b>in-vivo magnetic resonance imaging methods</b> . We have successfully implemented a refined high-resolution approach to imaging the transverse diffusion properties of human spinal cord in-vivo. This work reveals the internal architecture of the spinal cord white matter, not previously reported, and its distribution suggests that these diffusion results are driven by the <b>diffusion barrier spacing</b> . <b>Kurtosis results support the complexity of the extracellular diffusion pathways</b> as the primary determinant of these results. Prior work suggests that barrier spacing is largely a function of axon density, and indirectly related to the fiber diameter distribution. The imaging results also permit high-resolution identification of several white matter tracts, not otherwise visible in-vivo. We have also implemented <b>in-vivo human subject spinal cord myelin imaging</b> using an <b>inhomogeneous magnetization transfer (ihMT)</b> approach. Prior work with this method indicates that it is sensitive to myelin content, and not confounded by edema or diffusion barrier spacing. Thus, diffusion and ihMT methods combine to offer <b>independent assessment of axonal architecture (diffusion) and myelin content (ihMT)</b> . As both methods have been accomplished in-vivo in human subjects, this work will lead directly to characterization of axonal response to spinal cord injury in patients.					
15. SUBJECT TERMS Spinal cord injury, magnetic resonance imaging, diffusion, axonal injury, myelin content, reduced field of view, STEAM, inhomogeneous magnetization transfer, axonal diameter distribution, diffusion barrier spacing, diffusion kurtosis					
16. SECURITY CLASSIFICATION OF:			17. LIMITATION OF ABSTRACT	18. NUMBER OF PAGES	19a. NAME OF RESPONSIBLE PERSON
a. REPORT U	b. ABSTRACT U	c. THIS PAGE U			USAMRMC
			UU		19b. TELEPHONE NUMBER (include area code)

Table of Contents

	<u>Page</u>
Introduction.....	4
Body.....	4-11
Key Research Accomplishments.....	11
Reportable Outcomes.....	11
Conclusion.....	11-12
References.....	12
Appendices.....	12

## Introduction

In this year of the study, we focused on developing imaging techniques to characterize axon fiber structure and to assess myelin preservation in vivo. Both endeavors were successful, and both have yielded promising results that confirm our hypothesized ability to assess axonal and myelin status in-vivo in human subjects.

## Body

### **In-vivo high resolution high b-value diffusion imaging of the spinal cord.**

**Axon fiber structure** inferences derive from diffusion imaging of the spinal cord. The major challenges for human in-vivo diffusion imaging arise from the cord's small size, motion, and variations in magnetic susceptibility surrounding the spine that require reduced field of view approaches. Limited diffusion sensitivity (b-values) until now has prevented reliable detection of variations in axon diameter in vivo. In this work, we have pioneered an approach to obtaining very high b values for in vivo imaging and demonstrated sensitivity to axon fiber architecture in cross sectional imaging of the cord.

## Methods

### *Pulse Sequence*

All experiments were performed on a 3.0 T GE Signa HDx scanner (GE HealthCare, Waukesha, WI, USA) with maximum gradient strength of 40 mT/m and a maximum achievable slew rate of 150 T/m/s. An EPI sequence capable of diffusion-weighted (DW) imaging using twice-refocused spin echo (TRSE) was modified for a stimulated echo acquisition mode (STEAM) excitation. The spatial-spectral pulse that forms the first RF excitation pulse in the sequence was retained. The second and third 90° RF excitation pulses were modified from 180° in the TRSE sequence in the STEAM sequence, and occurred concurrently with slice selection gradients. With this change, the echo time (TE) was now the sum of the duration between the first and second RF pulses and the duration between the third RF pulse and the central *k*-space line in image acquisition.

Diffusion-weighting gradients were applied right before the second RF pulse and right after the third RF pulse. The mixing time (TM), defined as the duration between second and third RF pulses, was user-selectable with a maximum possible value of 2 seconds. Crushers designed to cause dephasing of up to  $8\pi$  radians were placed within the mixing period to retain only the longitudinal magnetization. This modified pulse sequence allowed the acquisition of DW images with b of up to  $\sim 31,000$  s/mm<sup>2</sup> when the diffusion time ( $\Delta$ ) = 2 s. The lower TE used by the STEAM sequence facilitated the use of longer TMs and, thus, longer diffusion times, with limited impact of signal decay due to T<sub>2</sub>\* relaxation.

### *Data Acquisition*

The STEAM DW imaging sequence was used to acquire axial images of the cervical spinal cord (C4-C5) in six healthy volunteers (3 female, age = 18 – 32 years), using an eight-channel cervical-thoracic-lumbar (CTL) phased-array RF receive coil, with the first three channels activated. In the first experiment, a range of twelve linearly-spaced *b*'s was selected with diffusion gradients placed in the right-to-left direction and maximum *b*-value of 1100 s/mm<sup>2</sup> for each  $\Delta$  = 76, 130, 230, 490, and 1000 ms. This data will be referred to as 'b1100' in the following text. The following imaging parameters were used: TR = 2500 – 4000 ms, TE = 42-60 ms, FOV = 12 cm, acquisition matrix = 96 frequency encodes  $\times$  48 phase-encoding steps, left-to-right frequency direction, phase FOV = 0.5, slice thickness = 10 mm. Spatial saturation bands were placed anterior and posterior to the slice of interest to allow the acquisition of a reduced FOV. All images were reconstructed to form 128  $\times$  128 matrices.

In the second experiment, only TM was progressively increased to increase the maximum *b*-value as diffusion time  $\Delta$  increased, while keeping all other diffusion-related parameters the same across  $\Delta$ s. For each  $\Delta$  = 250, 500, and 1000 ms, twelve images with diffusion sensitization perpendicular to the spinal cord, in the right-to-left direction, were acquired with the DW STEAM EPI pulse sequence, and the following imaging parameters: TR = 2500 – 4000 ms, TE = 60 ms, FOV = 12 cm, acquisition matrix = 96 frequency encodes  $\times$  48 phase-encoding steps (reconstructed matrices of 128  $\times$

128), left-to-right frequency direction, phase FOV = 0.5, slice thickness = 10 mm, with spatial saturation bands placed anterior and posterior to the slice and diffusion sensitization in the right-to-left direction. The maximum possible  $b$ -values corresponding to increasing  $\Delta$  were 3650, 7400, and 15000 s/mm<sup>2</sup>, with increased spacing between the higher  $b$ -values. This data will be referred to as the ‘bmax’ or ‘full’ dataset in the following text.

Raw data were saved for all acquisitions, along with reference data used for EPI phase correction of Nyquist ghosts and correction matrices used to accommodate  $k$ -space points sampled on the gradient ramps.

### Post-Processing

Tools for image reconstruction and post-processing were developed in-house using MATLAB (The MathWorks, Natick, MA, USA). Raw  $k$ -space data corresponding to each image were first corrected for variable-gradient sampling of  $k$ -space, followed by phase correction for constant and linear phase errors using the reference data acquired from a non-phase encoded acquisition and obtainable on the MRI scanner. Next, the low-pass Fermi filter, given by  $H_{i,j} = \frac{1}{1 + \exp(\frac{k_{i,j} - B}{A})}$  with  $A = 0.05$  and  $B = 0.8$ , was used to smooth  $k$ -space, followed by iterative Homodyne processing. All of these operations were carried out on individual excitations and receiver channel outputs. At this stage, the low-resolution (48×96) images were averaged across excitations. It was found that only one receiver channel contained most of the signal, and so the contributions from the other receiver channels were discarded. The final step involved interpolation to 64×128 matrices, yielding one image corresponding to each combination of  $b$ -value and diffusion time  $\Delta$ .

Each set of images (with the same  $\Delta$  and a range of twelve  $b$ -values) was processed separately. Post-processing began with a noise-floor reduction step, in which the noise was estimated by calculating the mean of the signal from a region of interest (ROI, 100 pixels) placed in the background on the five images weighted with the highest  $b$ -values. This number was subtracted from the entire set of twelve images to reduce the noise floor. Next, one ROI was chosen for each set of diffusion-weighted images, (a) to encompass the entire spinal cord (an ROI of ~80 pixels, i.e., ~700 mm<sup>3</sup> voxel), (b) to select only gray matter (GM, with an ROI of 8 pixels, i.e., a 70.3 mm<sup>3</sup> voxel) within the anterior columns, and (c) to select only white matter (WM, with an ROI of 8 pixels, i.e., a 70.3 mm<sup>3</sup> voxel) within the posterior funiculus.

For each volunteer, the signal decay curves obtained from the selected ROIs for a combination of  $b$  and  $\Delta$  were input to several fitting equations using a non-linear least-squares algorithm, including:

- (1) The mono-exponential (ME) signal decay model, given by  $S_b = S_0 e^{-b \cdot ADC}$ , where  $S_b$  is the signal within the ROI at a given  $b$ -value ( $b$ ),  $S_0$  is the signal at  $b \sim 0$  s/mm<sup>2</sup>,  $ADC$  is the apparent diffusion coefficient (ADC). Boundary conditions for the  $ADC$  were set at  $[10^{-8} - 10^{-1}]$ .
- (2) A bi-exponential (BE) signal decay model was employed, given by  $S_b = S_0 (f e^{-b \cdot ADC_f} + 1 - f e^{-b \cdot ADC_s})$ , where  $S_b$  is the signal within the ROI at a given  $b$ -value ( $b$ ),  $S_0$  is the signal at  $b \sim 0$  s/mm<sup>2</sup>,  $ADC_f$  and  $ADC_s$  are the ADCs of the fast and slowly decaying components, respectively, where the fraction of the fast-decaying component is denoted by  $f$ . Boundary conditions for  $f$ ,  $ADC_f$ , and  $ADC_s$  were set at  $[0 \ 1]$ ,  $[10^{-6} \ 10^{-1}]$ , and  $[10^{-8} \ 10^{-2}]$ , respectively.
- (3) The diffusional kurtosis (DK) decay model was employed, given by  $S_b = S_0 (e^{-b \cdot ADC + \frac{K_{app}}{6} (b \cdot ADC)^2})$ , where  $S_b$  is the signal within the ROI at a given  $b$ -value ( $b$ ),  $S_0$  is the DK signal at  $b \sim 0$  s/mm<sup>2</sup>,  $ADC$  is the apparent diffusion coefficient (ADC), and  $K_{app}$  is the excess kurtosis of the diffusion displacement probability function. Boundary conditions for  $K_{app}$  and  $ADC$  were set at  $[0 \ 10]$  and  $[0 \ 1]$ , respectively.

The stopping criterion for the three models was set to a residual error of  $10^{-12}$  or less. All models were implemented with MATLAB’s optimization toolbox, and  $S_0$  was also an unknown in each case.

### Results

**Figure 1** shows example images acquired *in vivo* using the diffusion-weighted STEAM pulse sequence on one volunteer, with  $b \sim 550$  s/mm<sup>2</sup> (top row) and the highest possible  $b$ -value ( $b_{max}$ , bottom row) for  $\Delta = 76$  ms (first column, with  $b_{max} \sim 1100$  s/mm<sup>2</sup>), 250 ms (second column, with  $b_{max} \sim 3650$  s/mm<sup>2</sup>), 500 ms (third column, with  $b_{max} \sim 7350$  s/mm<sup>2</sup>), and 1000

ms (fourth column, with  $b_{max} \sim 14750 \text{ s/mm}^2$ ). All images were reconstructed from the raw data files and are shown with identical window and level settings. As seen from the images with  $b \sim 550 \text{ s/mm}^2$ , the lower signal to noise ratio (SNR) is due to increasing TMs, but the diffusion images are visually consistent, even at the longest diffusion time of one second. The images in the right column were acquired with increasing  $\Delta$  and  $b$ , clearly showing increasing contrast between the anterior columns of gray matter and the surrounding white matter. It is also remarkable that enough signal is preserved even with  $\Delta = 1000 \text{ ms}$  and a large diffusion weighting factor of  $b \sim 14750 \text{ s/mm}^2$ . In this image, it is also possible to indicate the pixels containing the posterior columns of gray matter surrounding the posterior funiculus of white matter.

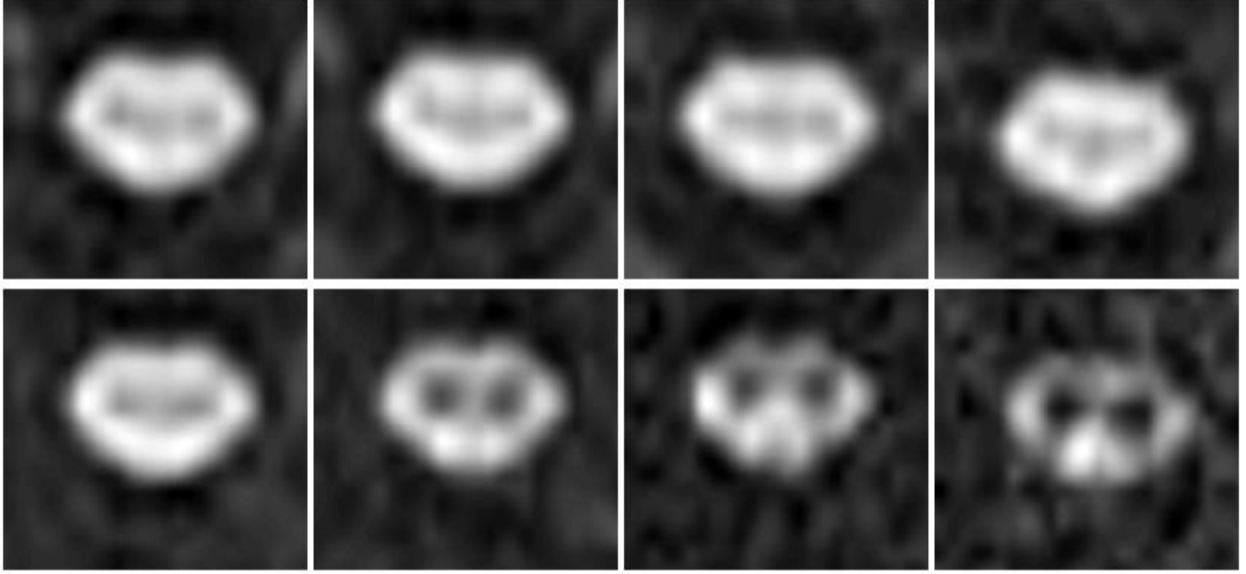


FIG 1: DW-STEAM images with  $b = 550 \text{ s/mm}^2$  (top row) and maximum possible  $b$ -values (bottom row) for diffusion times ( $\Delta$ ) of 76 ms (first column), 230-250 ms (second column), 490-500 ms (third column), and 1000 ms (fourth column). Window and level settings were adjusted independently for each image.

In order to compare the fitting results across a range of  $b$ -values larger than that used in the first experiment and to ascertain if the variations in fitting parameters were a function of  $\Delta$ , the ROI analysis was performed on a subset of the data obtained from the second experiment. Specifically, the signal decay curves corresponding to the entire cord and with  $b = 0 \sim 3500 \text{ s/mm}^2$  for diffusion times from 250 ms to 1000 ms were input to the fitting routines. This resulted in 12, 8, and 5 points for  $\Delta = 250, 500$ , and 1000 ms, respectively. This data will be referred to as the ‘b3500’ or ‘truncated’ dataset in the following text. As before, the truncated signal decay curves were fit to the ME, BE, and DK equations, and fitting parameters obtained were averaged across volunteers for comparison with the datasets using the full range of  $b$ .

Two-tailed pairwise statistical significance tests were performed to compare fitting parameters (a) across  $\Delta = 250 - 1000 \text{ ms}$  for the truncated (b3500) datasets, and (b) between WM and GM over  $\Delta = 250 - 1000 \text{ ms}$ , for the full and truncated datasets.

With the exception of one series of images acquired on one volunteer with  $\Delta = 490 \text{ ms}$  and  $b_{max} = 1100 \text{ s/mm}^2$ , all data from all six volunteers was used for further analysis. Of the three fitting equations, the BE fit yielded inconsistent parameters with large inter-subject variations when applied to ROIs comprising the entire cord, the WM and the GM, and was therefore excluded from further discussion.

Mono-exponential and diffusional kurtosis fitting equations introduced earlier were applied to the data acquired in experiment 1 (i.e., with  $b_{max} \sim 1100 \text{ s/mm}^2$ ). For the ROI comprising the entire cord, the ME fit yields a consistent ADC of  $5.66 \times 10^{-4} \text{ mm}^2/\text{s}$  over all volunteers, for  $\Delta = 76 = 1000 \text{ ms}$ . WM ADC was  $3.7 \times 10^{-4} \text{ mm}^2/\text{s}$ , while GM ADC was  $5.49 \times 10^{-4} \text{ mm}^2/\text{s}$ . The DK fit yielded average ADCs of  $6.85 \times 10^{-4} \text{ mm}^2/2$  with  $K_{app}$  of  $1.26 \pm 0.38$  over the range of  $\Delta$  with large inter-subject variation of  $K_{app}$  in data acquired within a single diffusion time, indicating lower consistency over this range of  $b$ -values. WM and GM ADC values were  $4.79 \times 10^{-4} \text{ mm}^2/\text{s}$  and  $6.91 \times 10^{-4} \text{ mm}^2/\text{s}$ , respectively, for the DK fit.  $K_{app}$  was  $2.05 \pm 0.35$  for WM and  $1.18 \pm 0.59$  for GM across  $\Delta$  with large variability across subjects within a single  $\Delta$ .

Data in experiment 2 was acquired by concurrently increasing both the range of  $b$ -values and diffusion time. Previous studies have shown that the ME fit is inadequate to explain signal decay with large  $b$ -ranges, leading to underestimation of ADC. The same was observed with this data, as ADC decreased from  $4.1 \times 10^{-4} \text{ mm}^2/\text{s}$  at  $\Delta = 250 \text{ ms}$  to  $1.6 \times 10^{-4} \text{ mm}^2/\text{s}$  at  $\Delta = 1000 \text{ ms}$ , for the ROI comprising the entire cord. Similarly, the DK fit showed ADCs from  $6.3 \times 10^{-4} \text{ mm}^2/\text{s}$  at  $\Delta = 250 \text{ ms}$  decreasing to  $3.0 \times 10^{-4} \text{ mm}^2/\text{s}$  at  $\Delta = 1000 \text{ ms}$ , and  $K_{app}$  decreasing from  $\sim 1.2$  at  $\Delta = 250 \text{ ms}$  to  $\sim 0.9$  at  $\Delta = 1000 \text{ ms}$ . **Figure 2a** is an example illustrating the use of the DK signal decay equation to fit the  $b_{max}$  data on one volunteer. The data points acquired using each  $\Delta$  were normalized to their corresponding  $S_0$  obtained using the ME equation on the signal attenuation curve of up to  $b \sim 1750 \text{ s/mm}^2$  for comparison on the same scale. This figure shows that the signal decay curve can be well approximated by the DK equation by a range of  $b$ -values extending only up to  $\sim 3000 \text{ s/mm}^2$ .

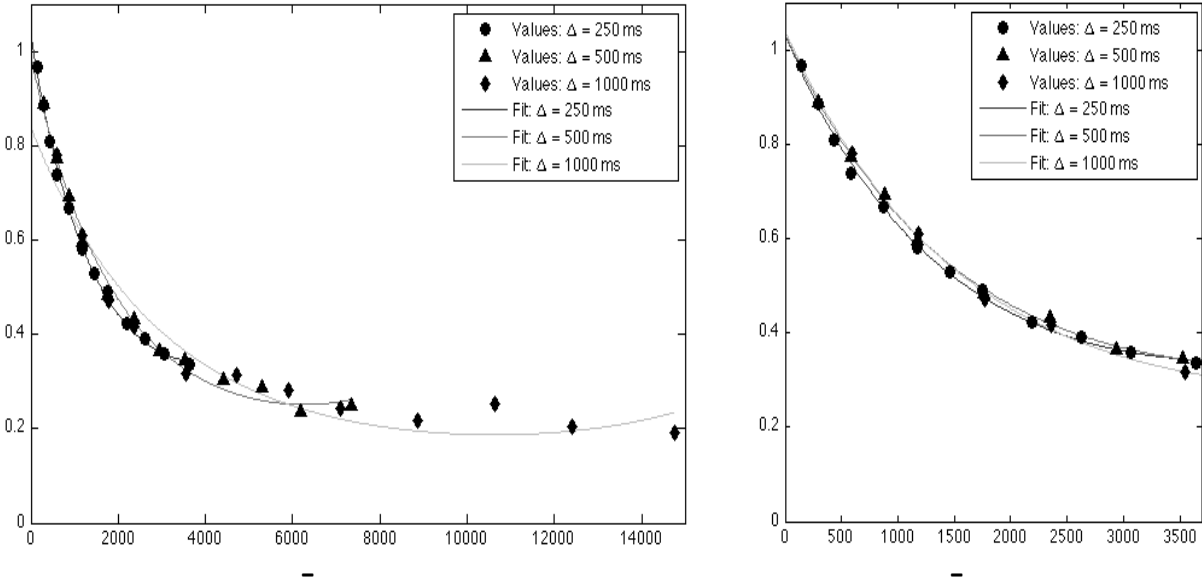


FIG 2: Data points (markers) and fitting results (solid lines) using the DK signal decay equation on ROIs comprising the whole cord, with (a) the full range of  $b$ -values of up to  $15000 \text{ s/mm}^2$ , and (b) with the truncated range of  $b$ -values of up to  $3650 \text{ s/mm}^2$ , for  $\Delta = 250 - 1000 \text{ ms}$ . Data acquired with each  $\Delta$  were normalized to the corresponding  $S_0$  obtained using the ME equation on the signal attenuation curve of up to  $b \sim 1750 \text{ s/mm}^2$  for comparison across  $\Delta$  and  $b$ -values, and are shown for one volunteer only.

Applying the fitting algorithms to smaller ROIs obtained from WM and GM highlighted the differences between these tissue types, especially as the  $\Delta$  and corresponding  $b$ -value range increased. For example, the ADCs obtained in the ME fit decreased from  $2.73 \times 10^{-4} \text{ mm}^2/\text{s}$  at  $\Delta = 250 \text{ ms}$  to  $0.62 \times 10^{-4} \text{ mm}^2/\text{s}$  at  $\Delta = 1000 \text{ ms}$  in WM, and from  $4.71 \times 10^{-4} \text{ mm}^2/\text{s}$  at  $\Delta = 250 \text{ ms}$  to  $3.14 \times 10^{-4} \text{ mm}^2/\text{s}$  at  $\Delta = 1000 \text{ ms}$  in GM. Similarly, ADCs in the DK fit decreased from  $4.23 \times 10^{-4} \text{ mm}^2/\text{s}$  to  $1.3 \times 10^{-4} \text{ mm}^2/\text{s}$  in WM and from  $6.7 \times 10^{-4} \text{ mm}^2/\text{s}$  to  $4.5 \times 10^{-4} \text{ mm}^2/\text{s}$  in GM (**Figure 3a**). Average values of kurtosis in WM were  $1.4 \sim 1.8$  and found to remain consistent across  $\Delta$  with large inter-subject variability in WM, while

decreasing across  $\Delta$  from 1.03 to 0.57 in GM (Fig. 3b). In general, the fitting parameters exhibited lower inter-subject standard deviation with increasing  $\Delta$  and  $b$ -ranges. There were statistically significant differences between GM and WM parameters, with  $p$ -values increasing as the range of  $b$ -values increased.

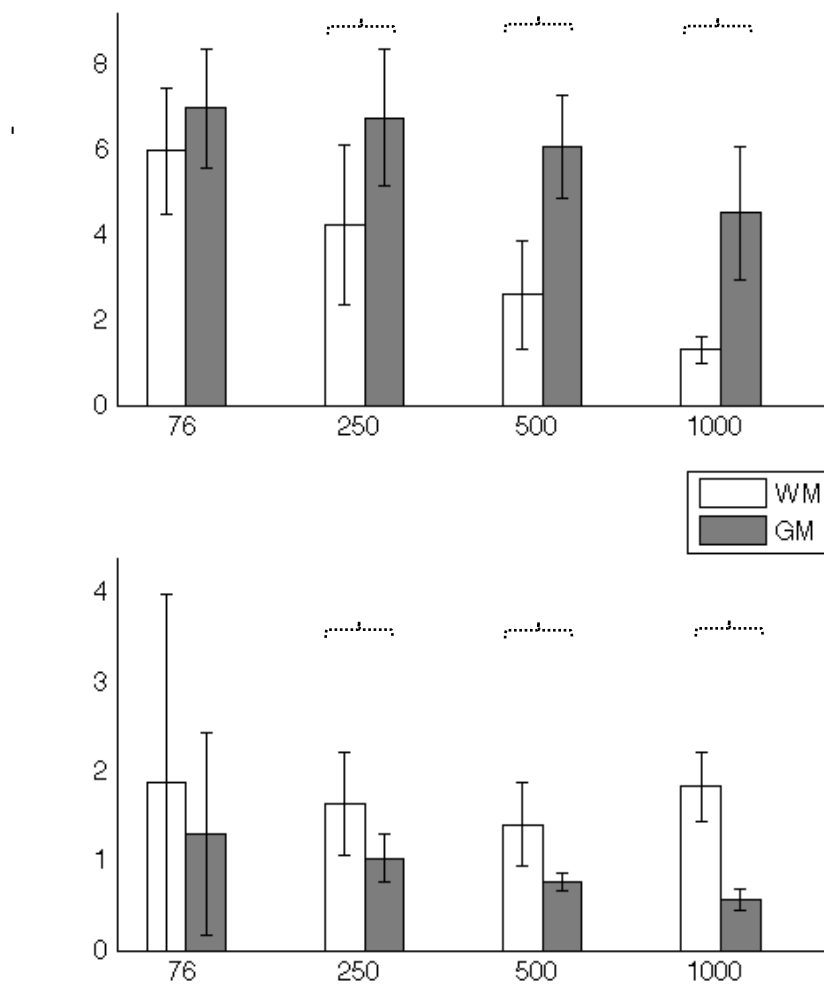


FIG 3: (a) shows ADC value, and (b) shows kurtosis values obtained with DK fit applied to signal decay with  $b$ -values of up to 15000 s/mm<sup>2</sup> in WM (first column, white bar) and GM (second column, gray bar). P-values (\* -  $p < 0.05$ , \*\* -  $p < 0.01$ , \*\*\* -  $p < 0.001$ ) indicate significant differences between WM and GM with increasing  $b$ -value range. Error bars are the standard deviations in parameters across subjects.



In general, the results of the first experiment indicate the need for a larger range of  $b$ -values to obtain consistent fitting parameters, while the results of the second experiment suggest that increasing  $b$ -ranges with increasing diffusion times may result in significantly different parameters. The third analysis was performed on a large and consistent range of  $b$ -values up to 3500 s/mm<sup>2</sup> for all diffusion times  $\Delta = 250 - 1000$  ms (Fig. 2b). Fitting the signal decay using the large ROIs showed less change in ADC, i.e., from  $4.1 \times 10^{-4}$  mm<sup>2</sup>/s at  $\Delta = 250$  ms to  $3.3 \times 10^{-4}$  mm<sup>2</sup>/s at  $\Delta = 1000$  ms using ME, and from  $6.2 \times 10^{-4}$  mm<sup>2</sup>/s at  $\Delta = 250$  ms to  $5.1 \times 10^{-4}$  mm<sup>2</sup>/s at  $\Delta = 1000$  ms in DK, with kurtosis constant at  $\sim 1.15$  (**Figure 4**). No significant difference in the fitting parameters was found over the range of diffusion times investigated in this study.

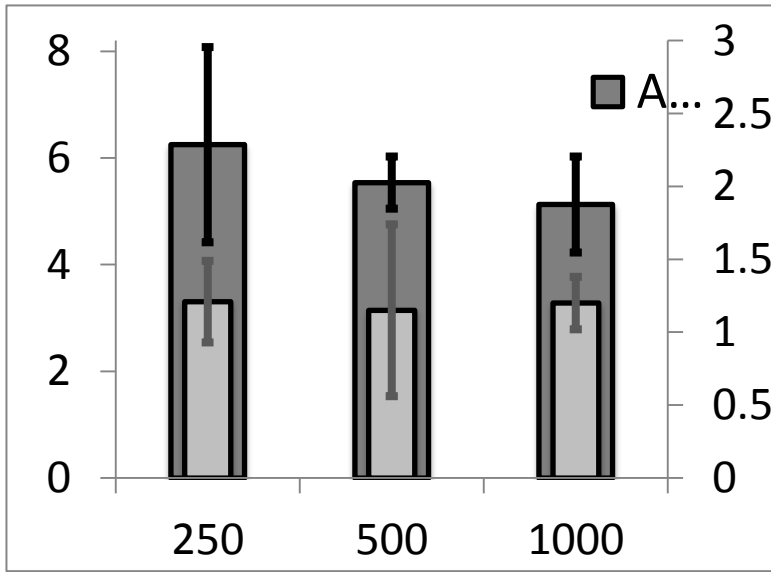


FIG 4 shows ADC (dark gray) and kurtosis (light gray) obtained with DK fit applied to signal decay with  $b$ -values of up to 3500 s/mm<sup>2</sup> in an ROI comprising the entire cord. P-values do not indicate any significant differences when compared pair-wise across diffusion time when the same range of  $b$ -values is used to fit the signal attenuation curves. Error bars show inter-subject standard deviations.

WM and GM ROI analyses using the ME fit over the truncated  $b$ -value range yielded WM ADCs of  $2.7 \times 10^{-4}$  mm<sup>2</sup>/s for  $\Delta = 250$  ms, decreasing to  $1.6 \times 10^{-4}$  mm<sup>2</sup>/s for  $\Delta = 1000$  ms. GM ADC remained nearly constant at  $4.63 \times 10^{-4}$  mm<sup>2</sup>/s across the range of diffusion times. The DK fit yielded WM ADCs of  $4.23 \times 10^{-4}$  mm<sup>2</sup>/s at  $\Delta = 250$  ms to  $2 \times 10^{-4}$  mm<sup>2</sup>/s at  $\Delta = 1000$  ms for WM, with GM ADC of  $\sim 7 \times 10^{-4}$  mm<sup>2</sup>/s over the range of  $\Delta$ . Similarly, kurtosis of GM stayed approximately constant at 0.92, however kurtosis of WM exhibited large variations across subjects and over  $\Delta$ , with no consistent trend visible. WM ADC values for the ME and DK fits were significantly different in the pair of  $\Delta = 250$  ms and  $\Delta = 1000$  ms, however kurtosis showed no significant differences across diffusion times. None of the GM parameters was significantly different across diffusion times.

**Discussion** These results are notable for several reasons. They highlight the difficulty of monoexponential fits in accurately reflecting the diffusion properties of the spinal cord, particularly when data is obtained with a wide range of  $b$  values. This has important technical implications for interpretation of diffusion data, extraction of fractional anisotropy,

kurtosis, and other higher order parameters from diffusion data. Since higher b value imaging emphasizes slower-diffusing components, this reveals cord structure not previously visible with in vivo MR techniques. Perhaps most readily applicable to human spinal cord injury, the results in Figure 1 demonstrate changing contrast across the white matter at higher b values. The dorsal columns and lateral corticospinal tracts have progressively relative preserved signal as the b values increase. This differential effect has not been previously reported in humans in vivo, although it was expected based on the known axonal architecture of the cord. These are regions of higher axonal density and consequently, smaller diffusion barrier spacing. This information is similar to that sought in q-space studies. However, this contrast is now observed directly from our acquired images, rather than extracted from, often noisy, q-space experiments.

Further work will be required to determine whether a reduced set of b values will provide sufficient data to infer changes in fiber diameters across the entire cord. Although large diameter fibers are crucial for fine touch, joint position sense and primary motor control, many serious deficits in patients with spinal cord injury result from loss of smaller fibers. This approach will permit us to monitor in vivo the changes in axon spacing and by implication, fiber diameter distribution in response to spinal cord injury.

### **Myelin Imaging:**

We implemented in inhomogeneous magnetization transfer (ihMT) method to detect myelin in spinal cord white matter. Previous approaches to estimating myelin content have relied on diffusion imaging, with problematic interpretation as reflecting myelin alone. Conventional magnetization transfer techniques are confounded by other effects that are commonly seen in CNS injury, including high sensitivity to edema. Thus, MT alone cannot reveal myelin content in the setting of spinal cord injury.

Conventional magnetization transfer (MT) imaging has been explored as a potentially sensitive marker to myelin in neurological disorders. However, MT is not a specific marker of white matter damage due to demyelination. We recently reported a technique to extract the ‘inhomogeneous’ component of MT (ihMT), which was shown to be specific to myelin in brain. The ihMT component is thought to come from more mobile macromolecular pools that cause asymmetrical line broadening about the center frequency, and can be extracted by applying MT saturation pulses with alternating (positive/negative) off-resonance frequencies. The goal of this study was to use the ihMT imaging technique to acquire a global myelin-specific image over the cervical spinal cord in the sagittal plane. A myelin-specific MT imaging technique may accurately and specifically reflect axonal damage in the event of spinal cord injury.

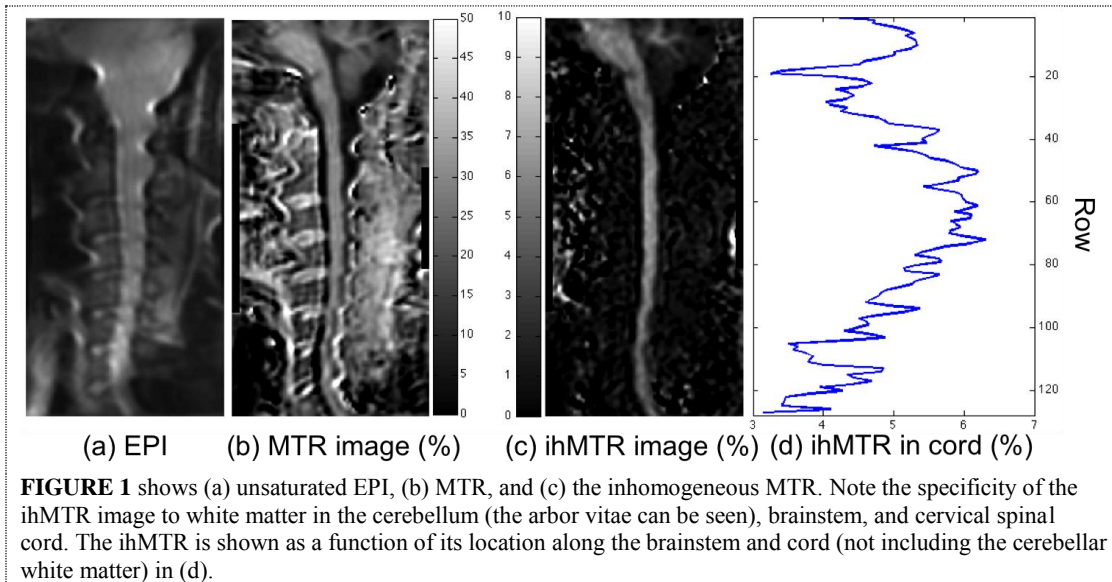
**Methods:** Images were acquired on a 3.0 T scanner (GE Healthcare, Waukesha, WI) using the upper half of a twelve-channel spine receiving coil. Inhomogeneous MT images were acquired by applying a pulsed saturation scheme for 500 ms, consisting of 500  $\mu$ s Hanning-shaped pulses applied every 1.5 ms with a  $\pm$  7.0 kHz frequency offset to acquire four images in each set, as follows: positive frequency offset (A), alternating dual frequency offset (B), negative frequency offset (C), alternating dual frequency offset (D). The average power of the MT pulses was 35 mG. Following the saturation, a single slice was acquired using single-shot spin-echo echo planar imaging (EPI) in the sagittal plane comprising the brainstem and cervical spinal cord, with the following imaging parameters: TR/TE = 2500/23 ms, FOV = 18 cm, phase FOV = 0.5, acquisition matrix  $96 \times 48$  (reconstructed to  $128 \times 64$ ), slice thickness = 10 mm, with 54 averages of each set and an additional eight averages of the unsaturated EPI image, for a total scan duration of  $\sim$  9 minutes. This protocol was followed on two healthy volunteers (female, 32 and 37 years).

The images were combined to yield the ihMT component image, given by:  $\text{ihMT} = (A + C) - (B + D)$ . Inhomogeneous MT ratios (ihMTR) were calculated by normalizing the ihMT images by the unsaturated EPI images. For comparison, the MT ratio (MTR) was also calculated using image ‘A’ as the saturated image. A mask was applied to select only the brainstem and spinal cord, and was used to calculate ihMTR as a function of position along these regions.

**Results:** Figure 1 demonstrates the result of this experiment on one volunteer. The unsaturated EPI image is shown in Fig. 1a, Fig. 1b shows the MT ratio, and the ihMT ratio is shown in Fig. 1c, clearly illustrating the specificity of this measure to myelin. The variation in ihMTR along the long axis of the cord and into the brainstem (Fig. 1d) is likely at least in part a function of partial volume effects. In the future, we propose to address this with a combination of careful alignment of the imaging axis along the long axis of the spinal cord, and use of thicker sections. Since only the WM appears to

demonstrate this ihMT effect, inclusion of adjacent CSF will not influence the results. Here the MT effect arises not only from the saturation of other macromolecules along with myelin in the cord but also from direct saturation effects. Similar results were seen on the second volunteer.

**Discussion:** Inhomogeneous MT imaging is clearly sensitive to regions within the cerebellum, brainstem, and cervical spinal cord. Its specificity to myelin in white matter is evidenced by the absence of signal in cerebellar gray matter, vertebrae, intervertebral disks, subcutaneous fat, and cerebrospinal fluid. Signal differences in ihMT between the spinal cord and the brainstem (particularly the medulla oblongata) are expected due to fractional differences in white matter between these regions. Although several averages were acquired to improve the signal to noise ratio (SNR), the ihMT quantification remained the same even with 1/4<sup>th</sup> the number of averages (data not shown). This, along with the



consistency of the values in two volunteers, indicates the robustness of the measure.

Disadvantages of the current acquisition are low SNR and large distortion due to EPI, which limited the imaging FOV to 18 cm in the sagittal plane. A move to the rapid acquisition with relaxation enhancement (RARE)

sequence is expected to improve both signal and robustness to  $B_0$  inhomogeneity-based artifacts, and allow better visualization of the entire spinal cord. Since most deficits from spinal cord pathology results from white matter dysfunction, a method for selectively imaging myelin will be a critical addition to imaging in trauma, demyelinating disease, and cord compression.

## Key Research Accomplishments

Implementation of high b-value in-vivo imaging

Demonstration of differential diffusion behavior in the human spinal cord

Diffusion results are consistent with the known high density of axon fibers, and hence diffusion barriers, in the dorsal columns and lateral corticospinal tracts

Implementation of inhomogeneous magnetization transfer (ihMT) in-vivo imaging.

Demonstration of high signal to noise sagittal imaging and reasonable imaging evidence of specificity for myelin

## Reportable Outcomes

The high b-value diffusion and the ihMT myelin imaging are both reportable. Both will be presented in oral or poster format at the International Society of Magnetic Resonance in Medicine meeting in Salt Lake City in April. We anticipate publishing these as separate manuscripts.

## Conclusions

The results of this work offer a pathway to direct imaging of diffusion barrier spacing, which we believe will be a specific marker of axonal injury. Loss of axons, or a shift to smaller diameter fibers, will increase barrier spacing and should be evident in these diffusion studies of the spinal cord. Our myelin imaging work complements the ultrashort TE (UTE) study reported last year. We now have at our disposal two promising approaches to detecting and ultimately quantifying myelin content in the spinal cord. The UTE method has been validated with excised specimens and myelin preparations, but will remain challenging to implement in vivo. Progress on this approach, including a switch to a zero TE (ZTE)

acquisition is described in the report from the University of Pennsylvania site. The ihMT method clearly works in vivo, and we are current refining it both for human subject imaging, and to validate the inference of myelin specificity and quantitative accuracy.

Together, we are well along toward our goal of characterizing axonal fiber structure and myelin content by completely independent means. Combining these will provide by far the most comprehensive measure to date of axonal damage after spinal cord injury.

#### **References**

None cited

#### **Appendices**

None